



OPEN Differentiation between multiple sclerosis and neuromyelitis optic spectrum disorders with multilevel fMRI features: A machine learning analysis

Xiao Liang^{1,2}, Qingwen Zeng³, Yanyan Zhu^{1,2}, Yao Wang^{1,2}, Ting He², Lin Wu^{1,2}, Muhua Huang^{2,4} & Fuqing Zhou^{1,2}✉

The conventional statistical approach for analyzing resting state functional MRI (rs-fMRI) data struggles to accurately distinguish between patients with multiple sclerosis (MS) and those with neuromyelitis optic spectrum disorders (NMOSD), highlighting the need for improved diagnostic efficacy. In this study, multilevel functional metrics including resting state functional connectivity, amplitude of low frequency fluctuation (ALFF), and regional homogeneity (ReHo) were calculated and extracted from 116 regions of interest in the anatomical automatic labeling atlas. Subsequently, classifiers were developed using different combinations of these selected features to distinguish between MS and NMOSD. Compared to models based on individual MRI features, support vector machine (SVM) and logistic regression (LR) models that integrated multilevel functional features such as RSFC, ALFF, and ReHo demonstrated the highest levels of performance on the testing cohorts (SVM, AUC = 0.857; LR, AUC = 0.929). Adding structural features of gray matter volume (GMV) data did not notably improve the classification performance of the machine learning models using multilevel rs-fMRI features. Notably, similar trends were observed across different brain templates, with models based on RSFC, ALFF, and ReHo yielding optimal performance. These findings suggest that utilizing multilevel fMRI features can effectively differentiate between MS and NMOSD patients.

Keywords Multiple sclerosis, Neuromyelitis optic spectrum disorders, Resting state functional magnetic resonance imaging, Machine learning

Multiple sclerosis (MS) and neuromyelitis optic spectrum disorder (NMOSD) are two relatively common autoimmune diseases with similar imaging characteristics. The latter has been considered as a subtype of MS in the past, and even called “Asian MS”. But in fact, there are differences in immunopathogenesis, clinical presentation, optimum treatment, and prognosis^{1–3}. When a NMOSD patient is misdiagnosed with MS, immunomodulatory medication therapy makes patients’ symptoms worsen¹. Therefore, to lessen the degree of disability, economic hardship, and social impact of patients with MS and NMOSD, correct diagnosis and suitable therapy are crucial.

The anti-aquaporin 4 (AQP4) antibody is a specific biomarker for neuromyelitis optic spectrum disorder (NMOSD) that helps differentiate between patients with multiple sclerosis (MS) and NMOSD. However, the sensitivity of the antibody test may vary, potentially resulting in false-negative results. Additionally, AQP4 antibody levels can decrease during NMOSD remission, posing challenges for detection in certain regions. In addition to AQP4 antibody testing, differential diagnosis is often based on specific MRI features seen in patients with MS and NMOSD². These features include long lesions of the optic nerve (at least half its length) (23/26, 88%) and spinal cord (at least 3 vertebral segments) (24/26, 92%) which are part of the diagnostic criteria for seronegative NMOSD⁴. Furthermore, unlike MS, MRI features like hypothalamic lesions, periventricular linear

¹Department of Radiology, The First Affiliated Hospital, Jiangxi Medical College, Nanchang University, Nanchang 330006, Jiangxi, China. ²Jiangxi Province Medical Imaging Research Institute, Nanchang 330006, Jiangxi, China.

³Department of General Surgery, The First Affiliated Hospital, Jiangxi Medical College, Nanchang University, Nanchang 330006, Jiangxi, China. ⁴Intervention Division Department of Radiology, The First Affiliated Hospital, Jiangxi Medical College, Nanchang University, Nanchang 330006, Jiangxi, China. ✉email: ndyfy02301@ncu.edu.cn

lesions, and periventricular lesions of the brainstem have been identified as specific to NMOSD^{5–7}. Moreover, recent imaging studies have shown that radiomic characteristics of lesions, morphological features, and white matter organization on routine imaging can also aid in distinguishing between MS and NMOSD patients^{8–11}. However, there remains a notable distinction between the lesion burden observed on routine imaging and the severity of symptoms or functional impairment in patients, which brings a gap or barrier to clinical practice.

Functional MRI (fMRI) is a valuable tool for investigating brain plasticity mechanisms and can be used to map the functional reorganization that occurs in MS and NMOSD in vivo, potentially addressing the 'clinical-radiological paradox'. Resting state fMRI (rs-fMRI) is commonly used in clinical research due to its ability to avoid cognitive or executive dysfunction interference by not requiring specific tasks. However, traditional statistical methods in rs-fMRI may not be sufficient to distinguish between MS and NMOSD patients. Recently, a study of machine-learning algorithms based on fMRI data have been used to distinguish MS patients from healthy controls (HCs) with 85.7% accuracy¹². These initial findings suggest a broader application of machine learning techniques to fMRI data in MS patients, highlighting the potential of rs-fMRI features in distinguishing between MS and NMOSD. Different types of features capture the distinct dimensions between MS and NMOSD patients, and some researchers have obtained encouraging results with over 85% accuracy by leveraging multilevel fMRI features for the differential diagnosis of various neurological diseases^{13–19}, such as Alzheimer's disease¹⁹ and major depressive disorder¹³. Additionally, Sun K et al¹³ also proposed that incorporating structural information has the potential to enhance the classification accuracy of multilevel fMRI classifiers.

The study aimed to explore the utility of multilevel fMRI features in distinguishing between patients with MS and NMOSD. Initially, the effectiveness of individual fMRI indices in classifying the diseases was examined. Subsequently, the research focused on identifying the optimal combination of multilevel fMRI indices for classification accuracy. Structural information was then incorporated to create multilevel functional-structural image joint features models, aiming to determine if these joint features could enhance the classifier's performance. Finally, the study assessed the consistency of findings through a repeatability analysis of Harvard–Oxford Atlas (HOA) templates. The goal of this study is to differentiate MS and NMOSD patients effectively using multilevel imaging features and enhance the clinical applicability of fMRI.

Materials and methods

Participants

Fifty-seven MS patients and 36 NMOSD patients were recruited from the First Affiliated Hospital, Jiangxi Medical College, Nanchang University between 2011 and 2023. The inclusion criteria for MS patients were: (i) age between 18 and 65 years, and (ii) clinically confirmed and reviewed by the revised diagnostic criteria of McDonald in 2017²⁰. The inclusion criteria for NMOSD patients were: (i) age between 18 and 65 years, and (ii) clinically confirmed and reviewed by the 2015 NMOSD international consensus diagnostic criteria². The exclusion criteria for patients were: (i) history of head injury or other neuropsychiatric diseases; (ii) presence of other autoimmune diseases; (iii) contraindications to MRI scanning; (iv) poor image quality.

This study adhered to the principles outlined in the Declaration of Helsinki, and approval for the study protocol was granted by the Human Research Ethics Committee of the First Affiliated Hospital of Nanchang University (Granted No.: 2021-4-074). Prior to participation, everyone provided written informed consent.

Clinical and neuropsychological assessments

All patients diagnosed with MS and NMOSD underwent evaluation using the following scales: (i) The Extended Disability Status Scale (EDSS) was used to assess cumulative disability status, with higher scores indicating more severe physical deficits (EDSS score ≤ 2.5 for low disability, between 2.5–6.5 for moderate disability, and EDSS score ≥ 6.5 for severe disability); (ii) The Paced Auditory Serial Addition Test (PASAT) was administered to measure impaired cognitive information processing speed; (iii) The Modified Fatigue Impact Scale (MFIS) was utilized to assess the impact of fatigue on cognitive, physical, and psychosocial functions in patients with MS and NMOSD.

MR imaging acquisition

Imaging data were obtained using a Trio 3.0T MRI scanner and an 8-channel phase-controlled head coil (Siemens, Munich, Germany). During the scan, each participant maintained a supine position, wore ear plugs, used foam pads to minimize head movement, closed their eyes, relaxed, and stayed awake. They were instructed not to engage in specific thoughts during the rs-fMRI scan. The rs-fMRI image acquisition was performed using an echo planar imaging sequence with gradient echo: repetition time (TR)/echo time (TE) = 2000/30 ms, matrix = 64×64 , field of view (FOV) = 210×210 mm², slice thickness = 4.00 mm, and 240 time points. Additionally, high-resolution 3D T1-weighted images were acquired with TR/TE = 1900/2.26 ms, matrix = 240×256 , FOV = 215×230 mm², slice thickness = 1.00 mm, and 176 sagittal slices.

Data preprocessing

The following preprocessing was performed on the MATLAB R2018b (Math Works, Inc.) platform using the DPARSF_V5.2 (<http://rfmri.org/DPARSF>) toolbox for the 3D-T1 and fMRI data of each subject: (i) removal of the first 10 time points; (ii) slice timing correction; (iii) head motion correction, we restricted the further analysis in participants with no more than 2.0° angular rotation on any axis or 2.0 mm translation; (iv) covariates such as linear drift, white matter signal, and cerebrospinal fluid were removed without global signal regression; (v) spatial normalization was conducted by first registering functional images to high-resolution T1 data, then segmenting and registering T1 images to the standard space of the Montreal Neurological Institute template space, and finally resampling to a voxel size of $3.0 \times 3.0 \times 3.0$ mm³; and (vi) the data were filtered to 0.01–0.1 Hz to attenuate respiration and other high-frequency physiological noises (except for amplitude of low-frequency

fluctuations (ALFF) calculation). In the present study, four types of features were extracted. It should be noted that the preprocessing for different types of feature calculations was different. The detailed preprocessing procedures for each type of fMRI metric were introduced in the Supplementary Methods.

Feature extraction

In this study, the regional homogeneity (ReHo), ALFF, and gray matter volume (GMV) maps were initially calculated using standard procedures. The GMV map was obtained after segmentation and then spatially smoothed (Gaussian kernel: 6 mm) for subsequent analysis and statistical purposes.

Subsequently, each of these maps was divided into 116 regions of interest (ROIs) based on the automated anatomical labeling (AAL) atlas. The ReHo, ALFF, or GMV values for each ROI were determined as the average ReHo, ALFF, or GMV value across all voxels within the ROI. To assess resting-state functional connectivity (RSFC), the average time series of each ROI was computed by averaging the rs-fMRI time series of all voxels within the ROI. Pearson correlation analysis was conducted on all ROI time series pairs, and the Fisher z transformation was applied to convert the correlation coefficients into z values. A total of 6670 Z -transformed correlation coefficients were used as the RSFC between all ROI pairs, plus 116 ReHo and 116 ALFF values, resulting in a total of 6902 multilevel resting state functional image features, and 116 GMV structural image features (Fig. 1).

Feature selection

All patients were randomly allocated into the training and testing cohorts in a 7:3 ratio. Subsequently, we filtered the optimal feature set from the training set. Initially, The features in the training cohorts are normalized by Z -score normalization. Then, we employed the Pearson rank correlation test to evaluate the linear correlation between individual features for redundancy elimination. Once two features have a stronger correlation, they will have a higher absolute value of the correlation coefficient. We selected one of the features for subsequent analysis when a Pearson correlation coefficient > 0.65 was found between each feature. Finally, least absolute shrinkage and selection operator (LASSO) regression was utilized for feature selection with non-zero coefficients as valuable predictors in each feature group. The weight coefficient of the final selected feature was retained. Given the higher dimensionality of RSFC compared to other feature types, in addition to the outlined feature selection process, further dimension reduction was conducted based on the number of RSFCs between different brain regions. Specifically, for the RSFCs retained after LASSO, the quantity of RSFCs associated with each brain region was documented. The greater the number of RSFCs linked to a specific brain region, the more closely that region was associated with distinguishing between MS and NMOSD patients. Brain regions with multiple RSFC features were selected, ultimately preserving the RSFC features between them.

Model building

Following feature selection, the study evaluated the discriminative ability of different types of features in distinguishing between patients with MS and NMOSD. Each type of feature captures unique aspects of the differences between MS and NMOSD, leading to the generation of 15 combinations. These combinations include: (i) ReHo, ALFF, RSFC single functional image features and GMV single structural image features; (ii) various multilevel functional image feature combinations such as ReHo + ALFF, ReHo + RSFC, ALFF + RSFC, ReHo + ALFF + RSFC; and (iii) multilevel functional image-structural image joint features combinations like ReHo + GMV, ALFF + GMV, RSFC + GMV, ReHo + RSFC + GMV, ReHo + ALFF + GMV, ALFF + RSFC + GMV, ReHo + ALFF + RSFC + GMV.

Then, we employed Python 3.7.12 Scikit-learn to develop machine learning classification models for each feature combination. The different performance of two machine learning classifiers, support vector machine (SVM) and logistic regression (LR), in different feature combinations was compared. Furthermore, all models were validated using the testing cohorts. The models' ability to discriminate was assessed using receiver operating characteristic (ROC) curves and area under the curve (AUC) values in the testing cohorts. Evaluation metrics such as accuracy, sensitivity, and specificity were also considered. To estimate the clinical usefulness of the prediction models, decision curve analysis (DCA) was performed to assess the net benefit of the prediction models in the testing cohorts. Furthermore, we implemented tenfold cross-validation (CV) to assess the models' performance and report the relevant performance metrics.

Repetitive experiment

To assess the consistency of study findings across different templates, the current study utilized not only the AAL template but also the Harvard Oxford Atlas (HOA). The HOA template divides the whole brain, excluding the cerebellum, into 112 regions, with a similar analysis approach to the AAL template. A comparison was made between the results obtained using these two templates, focusing on the selected brain regions and the classification outcomes.

Statistical analysis

We employed IBM SPSS Statistics (Version 21.0, USA) to assess the clinical variables. Categorical variables were compared using Chi-square tests, and quantitative variables were compared using t -tests or the Mann–Whitney U -test to assess the differences in clinical characteristics among patients. A significance level of $P < 0.05$ was applied for statistical significance.

To explore the relationship between discriminant brain regions and clinical symptoms in patients with MS and NMOSD, partial correlation analysis was conducted with age and sex as covariates ($P \times n < 0.05$, Bonferroni correction). The analysis considered clinical data such as PASAT scale scores, EDSS scale scores, MFIS scale scores, and disease duration in both MS and NMOSD patients.

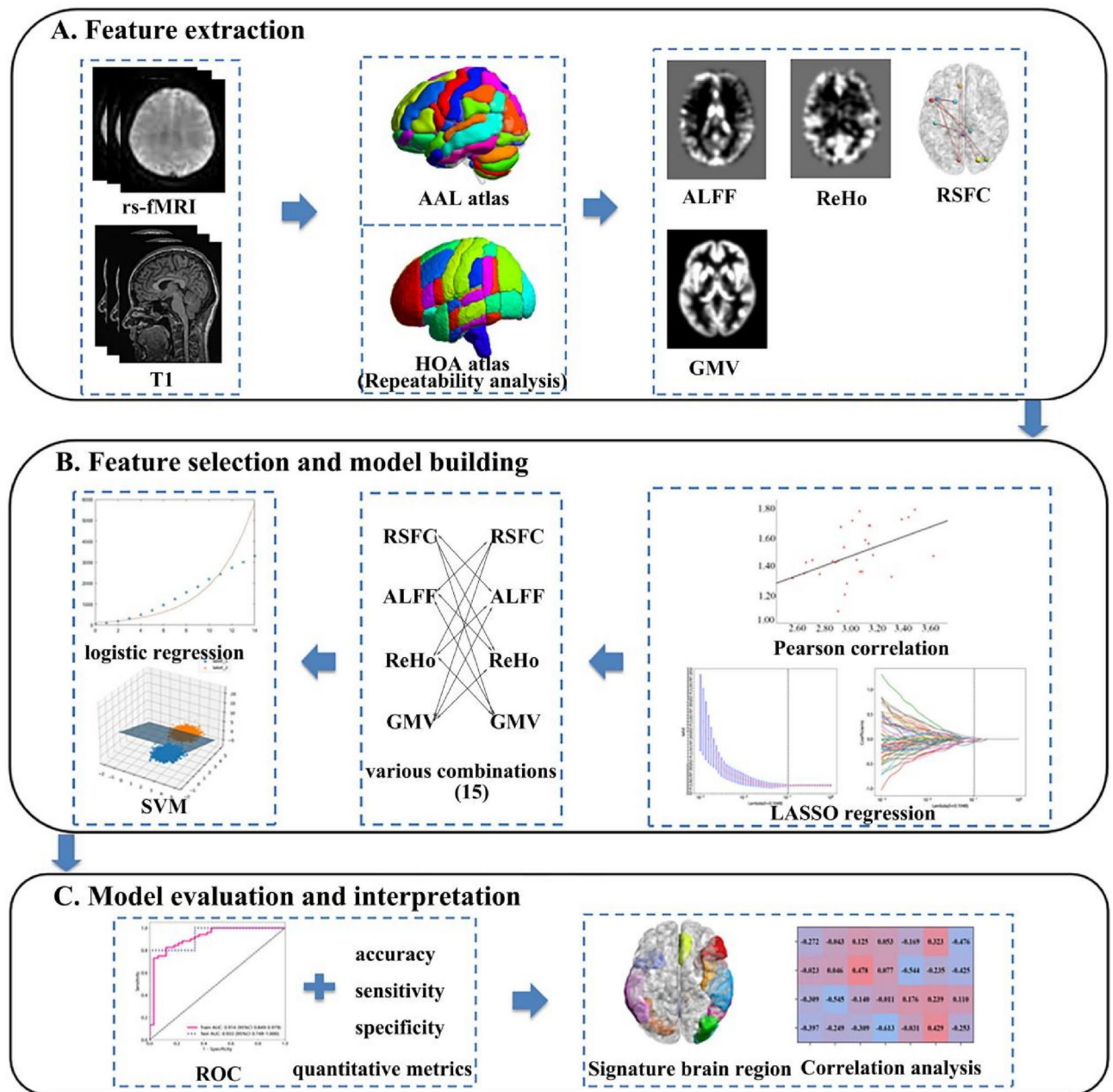


Fig. 1. Schematic outline of the whole study analysis procedure. Initially, multilevel functional image features (RSFC, ALFF, ReHo) and GMV structural image features were extracted using the AAL atlas (repetitive experiment was performed based on the feature set extracted from the HOA atlas). Subsequently, feature selection was carried out using the Pearson correlation test and LASSO regression to select crucial features and reduce dimensionality. Following this, SVM and logistic regression models were constructed using various combinations of features. The performance of the classifier was then evaluated using ROC curves and quantitative metrics. Finally, discriminative features were pinpointed, and correlation analysis was conducted to elucidate the underlying pathological mechanisms in MS and NMOSD patients. *Notes* RSFC, resting state functional connectivity; ALFF, amplitude of low-frequency fluctuations; ReHo, regional homogeneity; GMV, gray matter volume; AAL, Anatomical Automatic Labeling; HOA, Harvard–Oxford Atlas; LASSO, least absolute shrinkage and selection operator; SVM, support vector machine; ROC, receiver operating characteristic.

Results

Demographic and clinical data profiling

One MS patient was excluded due to head motion with greater than 2.0° angular rotation or 2.0 mm translation. Fifty-six MS patients and 36 NMOSD patients were entered into the final analysis. The demographic and clinical information are shown in Table 1. There were no significant differences between the two groups in terms of age,

	MS (N = 56)	NMOSD (N = 36)	P value
Gender (M/F)	17/39	7/29	0.265 ^a
Age, years (mean ± SD)	41.81 ± 11.48	40.92 ± 12.69	0.350 ^b
EDSS (median (IQR))	1.00 (1.50)	1.00 (1.50)	0.469 ^c
PASAT (median (IQR))	90.00 (26.50)	98.00 (24.75)	0.132 ^c
MFIS (mean ± SD)	8.77 ± 4.29	7.84 ± 5.65	0.035 ^b
Disease duration, months (median (IQR))	24.00 (30.50)	26.00 (76.25)	0.427 ^c

Table 1. Demographic and clinical characteristics of MS and NMOS patients. MS, multiple sclerosis; NMOSD, neuromyelitis optic spectrum disorders; EDSS, Expanded Disability Status Scale, PASAT, Paced Auditory Serial Addition Test; MFIS, Modified Fatigue Impact Scale; F, female; M, male; SD, standard deviation; IQR, inter-quartile range, N, number. ^achi-square test; ^b2-sample t test; ^cMann-Whitney U test.

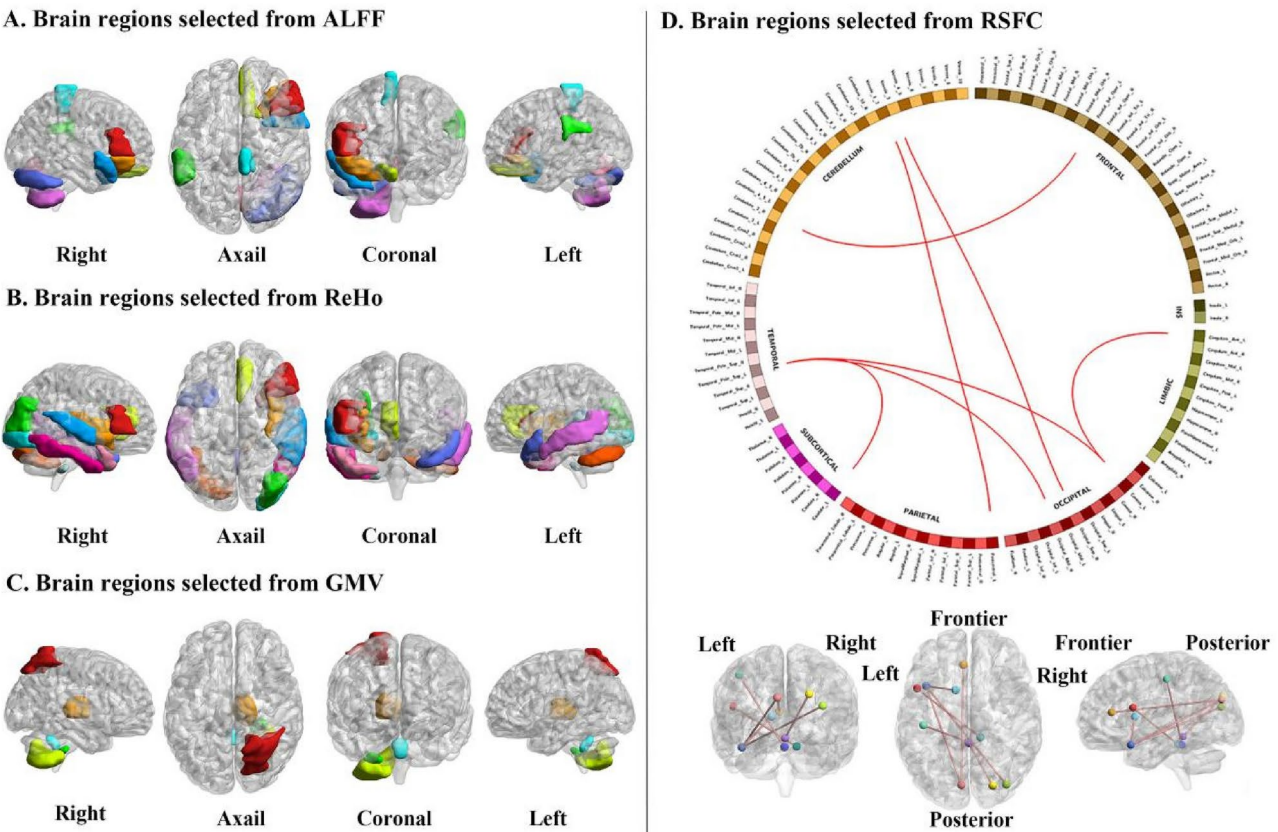


Fig. 2. The brain regions selected using the AAL template. (A) Brain regions selected from ALFF; (B) Brain regions selected from ReHo; (C) Brain regions selected from GMV; (D) Brain regions selected from RSFC. *Note* MS, multiple sclerosis; NMOSD, neuromyelitis optic spectrum disorders; AAL, Anatomical Automatic Labeling; RSFC, resting state functional connectivity; ALFF, amplitude of low-frequency fluctuations; ReHo, regional homogeneity; GMV, gray matter volume.

sex, EDSS scores, PASAT scores, and disease duration. In addition, there was a statistically significant difference in MFIS scores between MS and NMOSD patients ($P = 0.035 < 0.05$), suggesting that the overall fatigue levels of the MS patients were higher compared to the NMOSD patients.

Features selected for discriminating between MS and NMOSD

For the AAL template, following feature screening based on a Pearson correlation coefficient threshold of > 0.65 , a total of 3361 features (49%) were retained. This included 73 ALFF features (63%), 3211 RSFC features (48%), 12 GMV features (10%), and 65 ReHo features (56%). Subsequently, LASSO regression was applied for feature selection, identifying non-zero coefficients as valuable predictors within each feature group. Ultimately, 9 ALFF features, 14 ReHo features, 31 RSFC features, and 5 GMV features were retained for distinguishing between patients with MS and NMOSD (see Fig. 2 and Table 2). Among the 31 RSFCs (Supplementary Material Table S1), there were seven brain regions with 3 RSFCs and six brain regions with 2 RSFCs. Seven direct RSFCs between

	Brain area (AAL ID)	WASHU network	Weight coefficient
ALFF			
1	Frontal_Inf_Tri_R(14)	Salience	−0.065
2	Frontal_Inf_Orb_R(16)	Unknown	−0.037
3	Rectus_R(28)	Unknown	−0.045
4	Supra Marginal_L(63)	Affective network	−0.057
5	Paracentral_Lobule_R(70)	Sensorimotor network	0.029
6	Temporal_Pole_Sup_R(84)	Default mode network	−0.052
7	Cerebellum_Crus1_R(92)	Cerebellum	0.029
8	Cerebellum_8_R(104)	Cerebellum	0.037
9	Vermis_6(112)	Cerebellum	0.054
ReHo			
1	Frontal_Inf_Tri_R(14)	Salience	−0.029
2	Insula_R(30)	Cingular-opercular network	−0.055
3	Cingulum_Ant_R(32)	Default mode network	−0.055
4	Occipital_Mid_R(52)	Visual network	0.040
5	Occipital_Inf_R(54)	Visual network	0.004
6	Temporal_Sup_R(82)	Ventral attention network	0.030
7	Temporal_Pole_Sup_L (83)	Default mode network	0.069
8	Temporal_Mid_L(85)	Default mode network	0.014
9	Temporal_Pole_Mid_L(87)	Default mode network	−0.031
10	Temporal_Inf_R(90)	Unknown	0.021
11	Cerebellum_Crus1_L(91)	Cerebellum	−0.081
12	Cerebellum_3_R(96)	Cerebellum	0.088
13	Cerebellum_10_R(108)	Cerebellum	0.006
14	Vermis_4_5(111)	Cerebellum	−0.154
GMV			
1	Parietal_Sup_R(60)	Dorsal attention network	0.029
2	Cerebellum_10_R(108)	Cerebellum	0.020
3	Cerebellum_Inferior(104)	Cerebellum	−0.015
4	Thalamus_R(78)	Subcortical	−0.140
5	Vermis_10(116)	Cerebellum	0.010

Table 2. The ALFF, ReHo, and GMV features selected for discriminating between patients with MS and NMOSD using the AAL template. MS, multiple sclerosis; NMOSD, neuromyelitis optic spectrum disorders; L, left; R, right; AAL, Anatomical Automatic Labeling; ALFF, the amplitude of low-frequency fluctuation; ReHo, regional homogeneity; GMV, gray matter volume.

RSFC order	Brain area A	WASHU network	Brain area B	WASHU network	Weight coefficient
	Name (AAL ID)		Name (AAL ID)		
1	Frontal_Inf_Oper_L(11)	Frontoparietal network	Cerebelum_3_R(96)	Cerebellum	0.029
2	Cingulum_Ant_L(31)	Default mode network	Cuneus_L(45)	Visual network	0.039
3	Cuneus_L(45)	Visual network	Temporal_Pole_Sup_L(83)	Default mode network	0.002
4	Occipital_Sup_R(50)	Visual network	Vermis_3(110)	Cerebellum	−0.014
5	Occipital_Mid_R(52)	Visual network	Temporal_Pole_Sup_L(83)	Default mode network	0.006
6	Postcentral_L(57)	Sensorimotor network	Vermis_1_2(109)	Cerebellum	−0.021
7	Caudate_L(71)	Subcortical	Temporal_Pole_Sup_L(83)	Default mode network	−0.040

Table 3. The RSFCs features selected for discriminating between patients with MS and NMOSD using the AAL template. MS, multiple sclerosis; NMOSD, neuromyelitis optic spectrum disorders; L, left; R, right; RSFC, resting state functional connectivity; AAL, anatomical automatic labeling.

these 13 regions (≥ 2 RSFCs) were observed and therefore selected as the most discriminative RSFCs. Thus, after the above feature selection, we finally retained 7 RSFCs (Fig. 2 and Table 3, Supplementary Material Figure S1).

Moreover, the selected features were predominantly located in the default mode network (DMN) and cerebellum. Notably, ReHo features in the cerebellum played a significant role in distinguishing between MS and NMOSD patients. (Fig. 3).

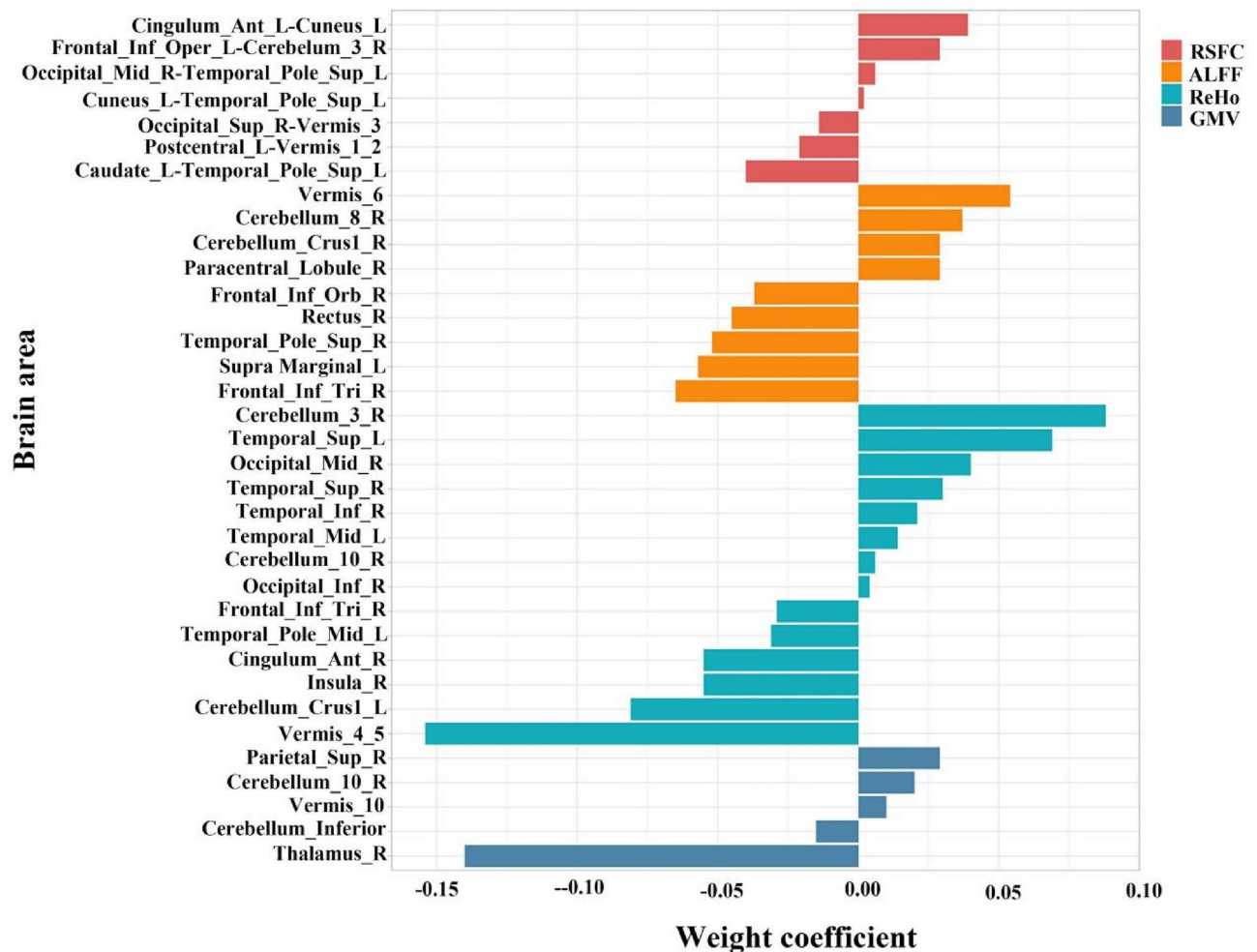


Fig. 3. The weight coefficients of ALFF, ReHo, GMV, and RSFC features were retained after selection using the AAL template. *Note* L, left; R, right; AAL, Anatomical Automatic Labeling; RSFC, resting state functional connectivity; ALFF, amplitude of low-frequency fluctuations; ReHo, regional homogeneity; GMV, gray matter volume.

The ability of the selected features to discriminate between MS and NMOSD

To determine the optimal model for distinguishing MS and NMOSD patients, we evaluated the performance of SVM and LR classifiers across 15 combination models (see Table 4, Fig. 4). Using the AAL template, we observed the following: (i) SVM and LR classifiers built with a single MRI feature had AUC ranges of 0.667 to 0.833 and 0.738 to 0.786, as well as ACC ranges of 0.667 to 0.812 and 0.739 to 0.833, respectively. (ii) The SVM and LR models incorporating RSFC, ALFF, and ReHo multilevel functional image features exhibited superior performance, achieving AUC values of 0.857 (95% confidence interval (CI) 0.618–1.000) and 0.929 (95% CI 0.762–1.000), along with ACC values of 0.818 and 0.909, respectively. These results outperformed models based on single functional or structural features. Furthermore, the model exhibited promising clinical usefulness (see Supplementary Material Figure S2-3). (iii) Combining functional and structural image features yielded AUC ranges of approximately 0.738 to 0.825 for SVM and 0.722 to 0.889 for LR classifiers, and ACC ranges of 0.696 to 0.846 and 0.652 to 0.875, respectively, indicating lower classification performance compared to models utilizing multilevel functional features (RSFC, ALFF, and ReHo). Furthermore, the results of tenfold cross-validation to assess the models' performance corroborated these findings (see Supplementary Material Table S6).

Repeatability analysis of HOA templates

For the HOA template, after feature screening with the same Pearson correlation coefficient threshold of >0.65 , 3104 features (47%) were retained, including 60 ALFF features (54%), 2951 RSFC features (47%), 13 GMV features (12%), and 80 ReHo features (71%). Following LASSO regression for feature selection, 8 ALFF features, 14 ReHo features, 4 GMV features, and 31 RSFC features were ultimately retained for the purpose of discriminating between patients with MS and NMOSD. The detailed information on the selected features was listed in Supplementary material Tables S2 and S3. Among these 31 RSFCs (see Supplementary Material Table S3), eight brain regions had three RSFCs, and five brain regions had two RSFCs. Seven direct RSFCs were

Models	Task	SVM		ACC		SN		SP		LR		ACC		SN		SP	
Modeling of features derived from single imaging metric		AUC (95%CI)		AUC		AUC (95%CI)		AUC		AUC (95%CI)		AUC		AUC (95%CI)		AUC	
RSFC	train	0.911(0.851–0.971)		0.862		0.870		0.848		0.762(0.660–0.864)		0.736		0.741		0.727	
	test	0.667(0.133–1.000)		0.667		1.000		0.333		0.778(0.291–1.000)		0.833		1.000		0.667	
	train	0.938(0.889–0.988)		0.857		0.814		0.926		0.804(0.693–0.916)		0.800		0.837		0.741	
	test	0.778(0.579–0.976)		0.739		0.643		0.889		0.738(0.527–0.949)		0.739		0.786		0.667	
ReHo	train	0.967(0.935–1.000)		0.922		0.872		1.000		0.828(0.737–0.919)		0.792		0.830		0.733	
	test	0.833(0.626–1.000)		0.812		0.800		0.833		0.733(0.469–0.998)		0.750		0.700		0.833	
GMV	train	0.873(0.793–0.952)		0.800		0.698		0.963		0.736(0.619–0.852)		0.700		0.558		0.926	
	test	0.706(0.466–0.947)		0.783		0.786		0.778		0.786(0.588–0.983)		0.783		0.714		0.889	
Modeling of features derived from multilevel fMRI imaging metrics																	
RSFC + ALFF	train	0.981(0.958–1.000)		0.919		0.868		1.000		0.889(0.800–0.979)		0.855		0.895		0.792	
	test	0.829(0.687–0.971)		0.742		0.579		1.000		0.820(0.670–0.970)		0.806		0.895		0.667	
RSFC + ReHo	train	0.997(0.992–1.000)		0.987		1.000		0.968		0.958(0.922–0.995)		0.886		0.917		0.839	
	test	0.800(0.525–1.000)		0.786		0.778		0.800		0.867(0.659–1.000)		0.857		1.000		0.600	
ALFF + ReHo	train	0.991(0.979–1.000)		0.963		0.980		0.935		0.902(0.831–0.973)		0.875		0.939		0.774	
	test	0.825(0.566–1.000)		0.846		0.875		0.800		0.825(0.526–1.000)		0.846		0.875		0.800	
RSFC + ALFF + ReHo (The proposed model)	train	0.995(0.987–1.000)		0.976		1.000		0.938		0.934(0.884–0.983)		0.866		0.820		0.938	
	test	0.857(0.618–1.000)		0.818		0.714		1.000		0.929(0.762–1.000)		0.909		1.000		0.750	
Modeling of features derived from functional imaging-structural imaging joint metrics																	
ALFF + GMV	train	0.957(0.891–1.000)		0.957		1.000		0.889		0.891(0.811–0.972)		0.871		0.860		0.889	
	test	0.738(0.531–0.946)		0.696		0.500		1.000		0.722(0.504–0.940)		0.652		0.429		1.000	
ReHo + GMV	train	0.992(0.978–1.000)		0.971		0.953		1.000		0.881(0.802–0.960)		0.857		0.837		0.889	
	test	0.738(0.502–0.974)		0.783		0.857		0.667		0.810(0.622–0.998)		0.826		0.714		1.000	
RSFC + GMV	train	0.971(0.937–1.000)		0.935		0.895		1.000		0.848(0.748–0.947)		0.806		0.737		0.917	
	test	0.772(0.601–0.943)		0.774		0.737		0.833		0.811(0.659–0.964)		0.774		0.684		0.917	
RSFC + ALFF + GMV	train	0.989(0.975–1.000)		0.949		0.938		0.968		0.925(0.868–0.982)		0.835		0.792		0.903	
	test	0.800(0.547–1.000)		0.786		0.667		1.000		0.889(0.695–1.000)		0.857		0.889		0.800	
SFC + ReHo + GMV	train	0.996(0.989–1.000)		0.987		0.979		1.000		0.890(0.820–0.960)		0.792		0.660		1.000	
	test	0.800(0.651–1.000)		0.812		0.900		0.667		0.867(0.657–1.000)		0.875		0.900		0.833	
ALFF + ReHo + GMV	train	0.997(0.992–1.000)		0.975		0.959		1.000		0.952(0.908–0.996)		0.912		0.939		0.871	
	test	0.825(0.574–1.000)		0.846		0.875		0.800		0.825(0.560–1.000)		0.846		0.875		0.800	
RSFC + ALFF + ReHo + GMV	train	0.997(0.992–1.000)		0.987		1.000		0.968		0.958(0.922–0.995)		0.886		0.917		0.839	
	test	0.800(0.525–1.000)		0.786		0.778		0.800		0.867(0.659–1.000)		0.857		1.000		0.600	

Table 4. The performance of the SVM and LR models built with different combinations among the four types of features using the AAL template, RSFC, resting-state functional connectivity, ALFF, amplitude of low-frequency fluctuations; ReHo, regional homogeneity; GMV, gray matter volume; ACC, accuracy; AUC, area under curve; CI, confidence interval; SN, sensitivity; SP, specificity; SVM, support vector machine; LR, logistic regression.

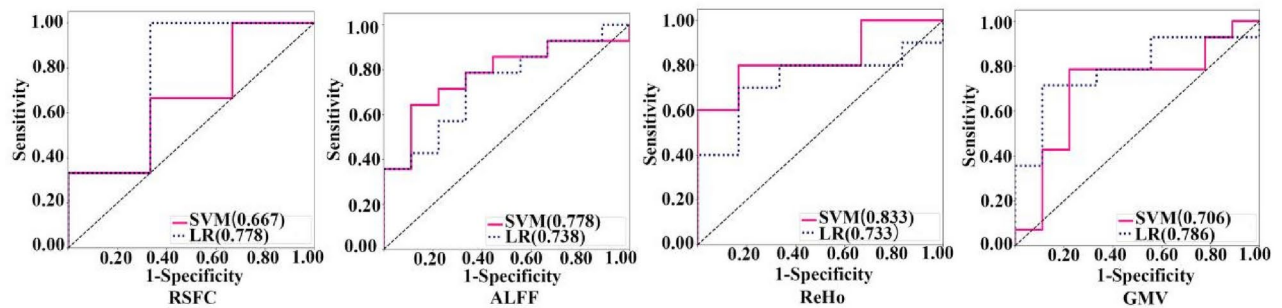
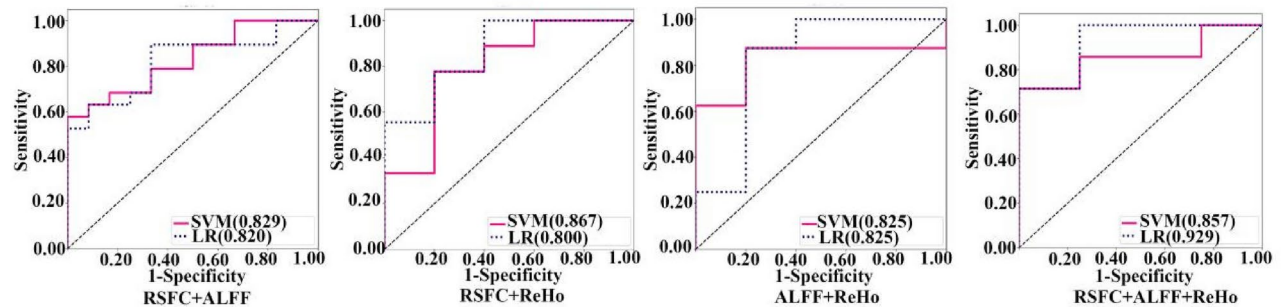
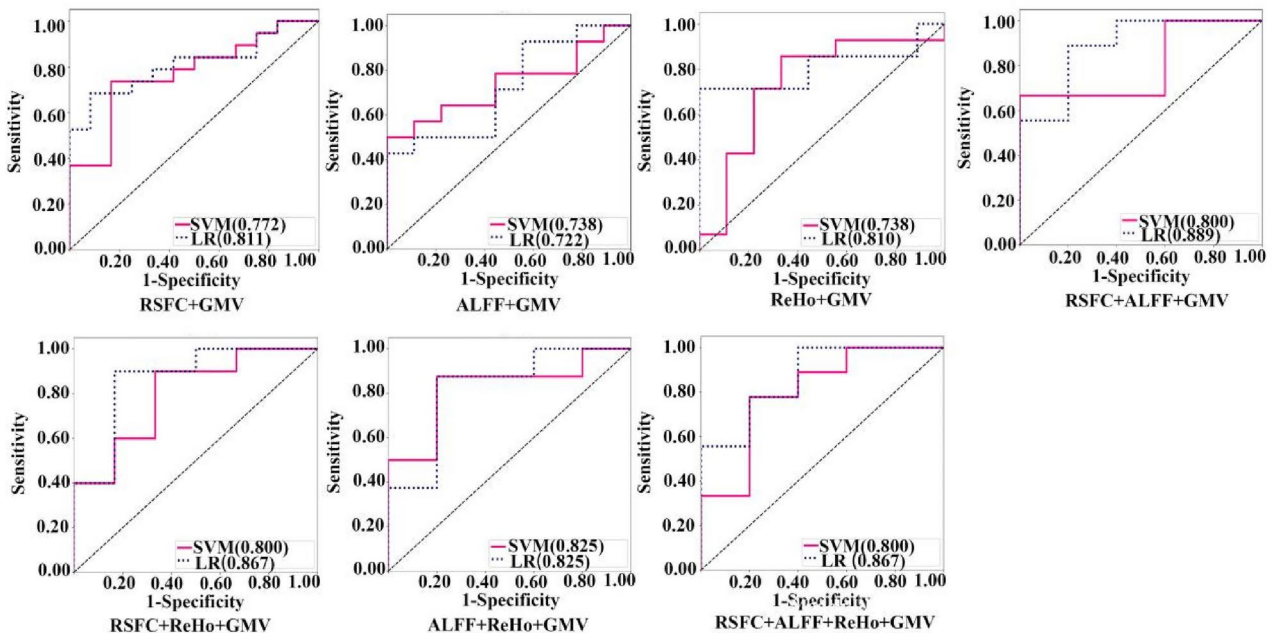
A. Modeling of features derived from single imaging metric**B. Modeling of features derived from multilevel fMRI imaging metrics****C. Modeling of features derived from functional imaging-structural imaging joint metrics**

Fig. 4. The ROCs of the SVM and LR models which were built with 15 combinations among the four types of features using the AAL templates. *Note* SVM, support vector machine; LR, logistic regression; AAL, Anatomical Automatic Labeling; RSFC, resting-state functional connectivity; ALFF, amplitude of low-frequency fluctuations; ReHo, regional homogeneity; GMV, gray matter volume.

identified among these 13 regions (with ≥ 2 RSFCs) and were selected as the most discriminative RSFCs. Thus, after the aforementioned feature selection, we ultimately retained seven RSFCs (see Supplementary Material Table S4).

For the HOA template, the classification performance was listed in Supplementary material Table S5. The results showed that the SVM and LR classifiers constructed by the combination of RSFC + ALFF + ReHo showed better classification performance in the testing cohorts (AUC = 0.875 (95% CI 0.679–1.000); AUC = 0.917 (95% CI 0.769–1.000)). It implied that the model built with RSFC + ALFF + ReHo was the most robust model for distinguishing patients with MS and NMOSD using the HOA template. Furthermore, the model exhibited

promising clinical utility as depicted in Supplementary material Figure S4-5. Furthermore, the results of tenfold cross-validation to assess the models' performance corroborated these findings (see Supplementary Material Table S7).

Correlation analysis

The partial correlation analysis results revealed that certain brain features (RSFC, ALFF, and ReHo) used to construct the optimal classifier exhibited significant correlations with clinical scores in both MS and NMOSD patient groups (see Supplementary Material Table S8-9). Notably, the ALFF value in the right inferior frontal gyrus orbital part demonstrated a negative relationship with the MFIS score in the MS group ($r = -0.337$, $P \times n < 0.05$, Bonferroni correction) (Fig. 4A). Similarly, the ALFF value in the right cerebellar 8 area was negatively correlated with the MFIS score in the NMOSD patient group ($r = -0.545$, $P \times n < 0.05$, Bonferroni correction) (Fig. 4B). Moreover, the RSFC values between the left inferior frontal gyrus opercular part and a region within the right cerebellum 3 area showed a significantly negative association with the PASAT score in the NMOSD patient group ($r = -0.544$, $P \times n < 0.05$, Bonferroni correction) (Fig. 4B). Additionally, the RSFC value between the left caudate nucleus and the left temporal pole superior temporal gyrus displayed a significantly negative correlation with the EDSS score in the NMOSD patient group ($r = -0.476$, $P \times n < 0.05$, Bonferroni correction) (Fig. 4B).

This study also found significant correlations between certain GMV features and the clinical presentations of patients with MS and NMOSD (Fig. 4A,B). Specifically, in the MS group, a negative correlation was observed between the MFIS score and the GMV value of the right cerebellum 10 area ($r = -0.371$, $P \times n < 0.05$, Bonferroni correction). Similarly, in the NMOSD group, a negative correlation was found between the GMV value of the right thalamus and the disease duration ($r = -0.613$, $P \times n < 0.05$, Bonferroni correction).

Furthermore, there were trend correlations between the final selected features and EDSS scores, PASAT scores, MFIS scores, and disease duration in both MS and NMOSD ($r = -0.425$ to 0.478 , $P < 0.05$, Bonferroni uncorrected) as shown in Fig. 5A,B.

Discussion

This study discovered that combining multilevel rs-fMRI imaging features machine learning classification that identifies MS and NMOSD with AUC and accuracy exceeding 80%, especially for the LR classifier (AUC: 0.929, ACC: 0.909). Additionally, the inclusion of GMV information did not significantly enhance the machine learning classification of multilevel rs-fMRI imaging features. The optimal model's features are predominantly located in relevant brain areas such as the cerebellum and DMN. Furthermore, the final selected features between MS and NMOSD patients are significantly associated with their respective clinical manifestations. These findings not only enhance the clinical utility of fMRI but also offer further evidence to elucidate the clinical impairments observed in MS and NMOSD patients.

Classification model

The differential diagnosis of patients with MS and NMOSD presents a challenge due to the possibility of misdiagnosis stemming from negative autoantibodies in cerebrospinal fluid and serum samples, as well as overlapping MRI features with MS. Recent studies have focused on utilizing data mining tools to enhance the analysis of brain image data for improved disease diagnosis^{8,21,22}. For instance, He et al.²³ utilized radiomics technology to extract radiomics features of lesions in T2-weighted images, effectively distinguishing between patients with MS and NMOSD. While this approach has shown promise in the differential diagnosis, interpreting numerical data derived from this analysis, such as texture and wavelet transform features, can be challenging in terms of their biological significance^{22,24,25}. Although rs-fMRI features are more straightforward to interpret than radiomics features, their lack of specificity limits their practical application. Eshaghi et al.²⁶ employed support vector machine classifiers to differentiate patients with MS and NMO with an accuracy of 88%, with the functional indicators included in this study limited to functional network connectivity, and structural information contributed the most to distinguishing disease. These findings suggest that rs-fMRI features can serve as neuroimaging markers for identifying MS, but their diagnostic efficacy may be limited due to the singular nature of the included images and inadequate exploration of fMRI data, potentially overlooking valuable information. Importantly, our findings reaffirm that individual functional imaging features alone are insufficient for distinguishing between patients with MS and NMOSD.

It is a reasonable assumption that combining multilevel functional image features can enhance classification performance. The RSFC captures the spatial correlation of neurophysiological activity across various brain regions²⁷. The ALFF indicates the intensity of spontaneous oscillatory functional activity in the brain²⁸. The ReHo measures the temporal consistency of neighboring regions in intrinsic neural activity²⁹. GMV reflects changes in the volume of gray matter³⁰. Utilizing different types of features can offer complementary insights to distinguish neurological differences between patients with MS and NMOSD.

As expected, combining RSFC, ALFF, and ReHo features led to improved classification performance compared to using a single MRI measure. However, classification models incorporating both fMRI and GMV indicators performed poorly on the test set, suggesting that structural indicators like GMV may interfere with fMRI indicators in distinguishing between MS and NMOSD patients. Additionally, the study evaluated the consistency of results using both the AAL and HOA brain templates. The findings demonstrated that the model constructed with RSFC, ALFF, and ReHo features was the most robust in distinguishing between MS and NMOSD patients.

Taken together, our study successfully developed an accurate and robust neural function models (RSFC, ALFF, and ReHo), demonstrating that MS and NMOSD can be accurately identified using machine learning with single-modal, multilevel rs-fMRI data.

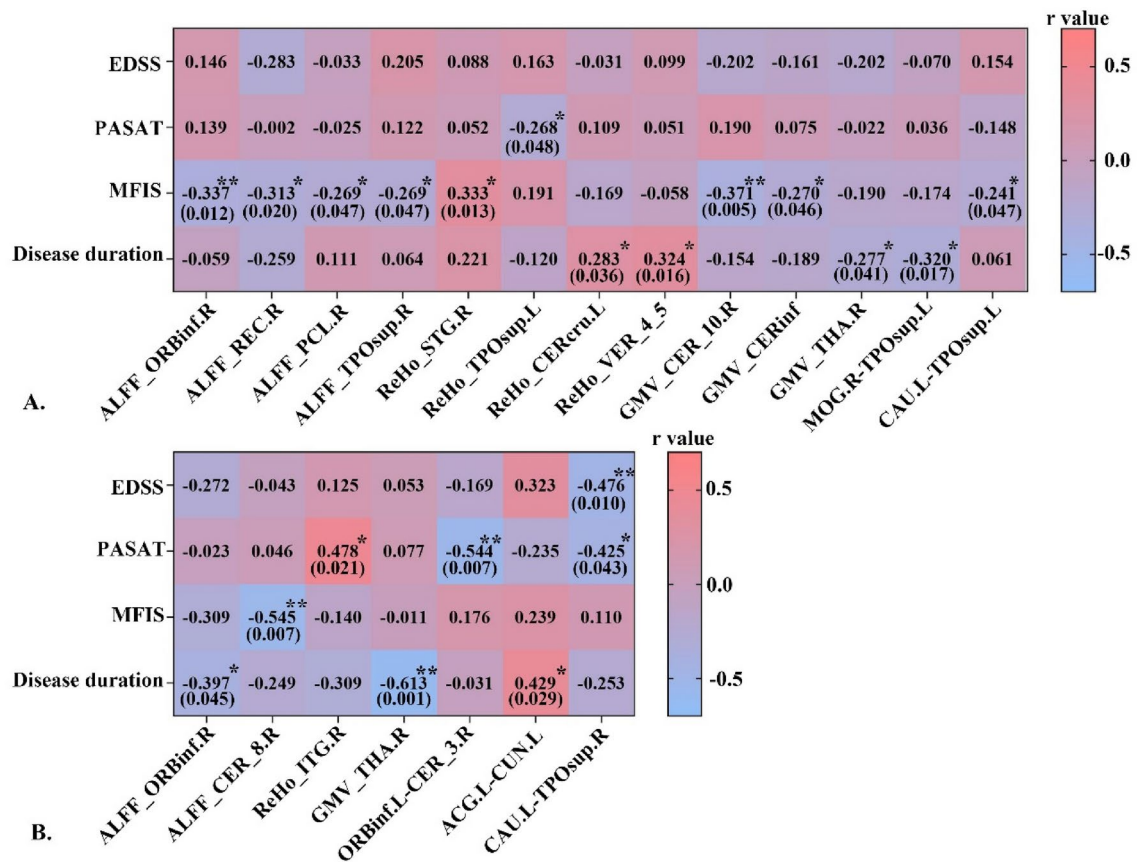


Fig. 5. The final selected features were significantly associated with EDSS scores, PASAT scores, MFIS scores and disease duration in MS (A) and NMOSD (B) groups. Note *, $P < 0.05$, $P \times n > 0.05$, Bonferroni correction; **, $P < 0.05$, $P \times n < 0.05$, Bonferroni correction; RSFC, resting-state functional connectivity; ALFF, amplitude of low-frequency fluctuations; ReHo, regional homogeneity; GMV, gray matter volume; EDSS, Expanded Disability Status Scale; PASAT, Paced Auditory Serial Addition Test; MFIS, Modified Fatigue Impact Scale; L, left; R, right; ORBinf, the inferior frontal gyrus orbital part; REC, the cerebellum; PCL, the paracentral lobule; TPOsup, the temporal pole: superior temporal gyrus; STG, the superior temporal gyrus; VER, the vermis; THA, the thalamus; MOG, the middle occipital gyrus; CAU, the caudate nucleus; ITG, the inferior temporal gyrus; ACG, the anterior cingulate and paracingulate gyri; CUN, the cuneus.

Different brain parcellation schemes may generate ROIs with distinct sizes and locations, leading to unique feature representations that influence classification performance. The primary aim of the AAL atlas was to provide a standard anatomical reference for fMRI data. However, the borders of each ROI in the atlas were delineated using sulcal landmarks, which exhibited poor consistency with cytoarchitectonic borders^{31,32}, resulting in variable sulcal and gyral patterns³². In contrast, the HOA atlas incorporates information on sulcal and gyral geometry³³, potentially offering a better reflection of individual variability. This study compared the consistency of results obtained from different templates, thereby demonstrating the robustness of the findings. However, due to the similarities in spatial resolution between HOA and AAL, the information extracted from these atlases may also exhibit limitations. However, finer segmentation schemes may involve small sample sizes paired with high-dimensional features, leading to potential overfitting of the model. Consequently, future studies utilizing larger datasets or multi-center data collections in conjunction with more refined segmentation schemes may enhance the robustness of the results.

The relationship of multilevel functional imaging features and clinical impairments

The features screened between the MS and NMOSD group covered a wide range of brain network areas, but they were mainly distributed in the cerebellum and DMN related brain regions. The cerebellum integrates multiple circuits throughout the brain and is involved in motor, cognitive, and emotional functions³⁴. Extensive changes in cerebellar structure and function had been reported in both MS^{35,36} and NMOSD^{37,38} patients, but most studies only focused on local cerebellar gray matter volume changes, and the sensitivity to distinguish diseases was low. Recent studies characterized convergent and divergent alterations in within-cerebellar and cerebello-cerebral morphological and functional connectivity in MS and NMOSD. The results showed that functional connectivity had the potential to distinguish MS from NMOSD³⁹. These differences are consistent with the findings of our study, suggesting that abnormal changes in cerebellar function may be one of the most potent biomarkers. Surprisingly, our study found that the RSFC values between the left inferior frontal gyrus

opercular part and a region within the right cerebellum had significantly negative correlations with the PASAT scores. Previous studies had also shown the abnormalities in brain-cerebellar functional connectivity are often associated with emotional and cognitive impairments.

The DMN is thought to be associated with the clinical symptomatology of several brain disorders and might have increased vulnerability to pathology due to hypothesized high oxygen consumption and blood flow⁴⁰. Neurovascular uncoupling has been recently described as a possible mechanism of brain dysfunction in severely impaired MS⁴¹ and NMOSD⁴¹ patients, and it might account for the reduced rs-fMRI activity of the DMN. Conversely, some studies have observed a higher RSFC in DMN in patients with MS⁴² and NMOSD⁴³ because they enroll a high proportion of cognitively preserved patients, probably shifting the balance towards a pattern of increased RSFC. Moreover, our study discovered that the RSFC values between the left caudate nucleus and the left temporal pole superior temporal gyrus had significantly negative correlations with the EDSS scores. Taken together, these findings suggest that the DMN might be another potential core area for further understanding of the pathophysiology of MS and NMOSD patients.

There are some limitations in this study. First, this study only used a single central data set for analysis without verification of the model's generalization with external data sets. Second, the methodology for calculating ReHo, ALFF, and GMV values involves averaging voxel values within each ROI, which may be sensitive to outliers due to the use of mean values. Third, while the study explored the potential of structural data to enhance the classification performance of the multilevel rs-fMRI model, it only focused on gray matter volume. Future research could consider incorporating indexes such as white matter volume and white matter fiber tract connectivity.

Conclusion

We developed a SVM and LR classifiers, which demonstrated high accuracy and predictive performance based on multilevel rs-fMRI features for differentiating MS and NMOSD. This significantly enhances the practical applicability of fMRI. However, to validate the generalizability of our model and explore the feasibility of incorporating additional structural information, external datasets are still required.

Data availability

The data supporting the findings of this study are available from the First Affiliated Hospital of Nanchang University. However, restrictions apply to the availability of these data as they were used under license for the current study and are not publicly available. Data can be obtained from the corresponding author upon reasonable request and with permission from the First Affiliated Hospital of Nanchang University.

Received: 27 June 2024; Accepted: 24 December 2024

Published online: 14 January 2025

References

- Kumpfel, T. et al. Update on the diagnosis and treatment of neuromyelitis optica spectrum disorders (NMOSD)—Revised recommendations of the Neuromyelitis Optica Study Group (NEMOS). Part II: Attack therapy and long-term management. *J. Neurol.* **271**(1), 141–176 (2024).
- Wingerchuk, D. M. et al. International consensus diagnostic criteria for neuromyelitis optica spectrum disorders. *Neurology* **85**(2), 177–189 (2015).
- Dobson, R. & Giovannoni, G. Multiple sclerosis: A review. *Eur. J. Neurol.* **26**(1), 27 (2019).
- Hyun, J. W. et al. Evaluation of the 2015 diagnostic criteria for neuromyelitis optica spectrum disorder. *Neurology* **86**(19), 1772 (2016).
- Nakajima, H. et al. Anti-aquaporin-4 antibody-positive neuromyelitis optica presenting with syndrome of inappropriate antidiuretic hormone secretion as an initial manifestation. *Case Rep. Neurol.* **3**(3), 263–267 (2011).
- Downer, J. J. et al. Diagnosis of neuromyelitis optica (NMO) spectrum disorders: Is MRI obsolete? *Neuroradiology* **54**(4), 279–285 (2012).
- Kim, W. et al. Characteristic brain magnetic resonance imaging abnormalities in central nervous system aquaporin-4 autoimmunity. *Mult. Scler.* **16**(10), 1229–1236 (2010).
- Luo X, Li H, Xia W, et al. Joint radiomics and spatial distribution model for MRI-based discrimination of multiple sclerosis, neuromyelitis optica spectrum disorder, and myelin-oligodendrocyte-glycoprotein-IgG-associated disorder. *Eur Radiol* (2023).
- Cortese, R. et al. Differentiating multiple sclerosis from AQP4-neuromyelitis optica spectrum disorder and MOG-antibody disease with imaging. *Neurology* **100**(3), e308–e323 (2023).
- Jurynczyk, M. et al. Elucidating distinct clinico-radiologic signatures in the borderland between neuromyelitis optica and multiple sclerosis. *J. Neurol.* **269**(1), 269–279 (2022).
- Huang, J. et al. Multi-parametric MRI phenotype with trustworthy machine learning for differentiating CNS demyelinating diseases. *J. Transl. Med.* **19**(1), 377 (2021).
- Sacca, V. et al. Evaluation of machine learning algorithms performance for the prediction of early multiple sclerosis from resting-state fMRI connectivity data. *Brain Imaging Behav.* **13**(4), 1103–1114 (2019).
- Sun, K. et al. A two-center radiomic analysis for differentiating major depressive disorder using multi-modality MRI data under different parcellation methods. *J. Affect. Disord.* **300**, 1–9 (2022).
- Liu, G. et al. Identifying individuals with attention-deficit/hyperactivity disorder based on multisite resting-state functional magnetic resonance imaging: A radiomics analysis. *Hum. Brain Mapp.* **44**(8), 3433–3445 (2023).
- Wei, W. et al. Analyzing 20 years of resting-state fMRI research: Trends and collaborative networks revealed. *Brain Res.* **1822**, 148634 (2024).
- Chen, Y. et al. The diagnostic performance of machine learning based on resting-state functional magnetic resonance imaging data for major depressive disorders: a systematic review and meta-analysis. *Front. Neurosci.* **17**, 1174080 (2023).
- Teng, J. et al. Brain disease research based on functional magnetic resonance imaging data and machine learning: a review. *Front. Neurosci.* **17**, 1227491 (2023).
- de Vos, F. et al. A comprehensive analysis of resting state fMRI measures to classify individual patients with Alzheimer's disease. *Neuroimage* **167**, 62–72 (2018).

19. Dai, Z. et al. Discriminative analysis of early Alzheimer's disease using multi-modal imaging and multi-level characterization with multi-classifier (M3). *Neuroimage* **59**(3), 2187–2195 (2012).
20. Thompson, A. J. et al. Diagnosis of multiple sclerosis revisions of the McDonald criteria. *Lancet Neurol.* **2017**, S1419424382 (2017).
21. Yan, Z. et al. Interpretable and intuitive machine learning approaches for predicting disability progression in relapsing-remitting multiple sclerosis based on clinical and gray matter atrophy indicators. *Acad. Radiol.* **31**, 2910 (2024).
22. Tavakoli, H., Pirzad, J. G. & Sedaghat, A. Investigating the ability of radiomics features for diagnosis of the active plaque of multiple sclerosis patients. *J. Biomed. Phys. Eng.* **13**(5), 421–432 (2023).
23. He, T. et al. MS or not MS: T2-weighted imaging (T2WI)-based radiomic findings distinguish MS from its mimics. *Mult. Scler. Relat. Disord.* **61**, 103756 (2022).
24. Yan, Z. et al. Quantitative susceptibility mapping-derived radiomic features in discriminating multiple sclerosis from neuromyelitis optica spectrum disorder. *Front. Neurosci.* **15**, 765634 (2021).
25. Peng, Y. et al. Prediction of unenhanced lesion evolution in multiple sclerosis using radiomics-based models: a machine learning approach. *Mult. Scler. Relat. Disord.* **53**, 102989 (2021).
26. Khajetash, B. et al. Introducing radiomics model to predict active plaque in multiple sclerosis patients using magnetic resonance images. *Biomed. Phys. Eng. Express* **9**(5), 055004 (2023).
27. van den Heuvel, M. P. & Hulshoff, P. H. Exploring the brain network: A review on resting-state fMRI functional connectivity. *Eur. Neuropsychopharmacol.* **20**(8), 519–534 (2010).
28. Zang, Y. F. et al. Altered baseline brain activity in children with ADHD revealed by resting-state functional MRI. *Brain Dev.* **29**(2), 83–91 (2007).
29. Zang, Y. et al. Regional homogeneity approach to fMRI data analysis. *Neuroimage* **22**(1), 394–400 (2004).
30. Bonacchi, R. et al. Association of age at onset with gray matter volume and white matter microstructural abnormalities in people with multiple sclerosis. *Neurology* **97**(20), e2007–e2019 (2021).
31. Ota, K. et al. A comparison of three brain atlases for MCI prediction. *J. Neurosci. Methods* **221**, 139–150 (2014).
32. Tzourio-Mazoyer, N. et al. Automated anatomical labeling of activations in SPM using a macroscopic anatomical parcellation of the MNI MRI single-subject brain. *Neuroimage* **15**(1), 273–289 (2002).
33. Desikan, R. S. et al. An automated labeling system for subdividing the human cerebral cortex on MRI scans into gyral based regions of interest. *Neuroimage* **31**(3), 968–980 (2006).
34. O'Reilly, J. X. et al. Distinct and overlapping functional zones in the cerebellum defined by resting state functional connectivity. *Cereb. Cortex* **20**(4), 953–965 (2010).
35. Schoonheim, M. M. et al. The cerebellum and its network: Disrupted static and dynamic functional connectivity patterns and cognitive impairment in multiple sclerosis. *Mult. Scler.* **27**(13), 2031–2039 (2021).
36. Tona, F. et al. Role of cerebellar dentate functional connectivity in balance deficits in patients with multiple sclerosis. *Radiology* **287**(1), 267–275 (2018).
37. Han, Y. et al. Functional connectivity alterations in neuromyelitis optica spectrum disorder: Correlation with disease duration and cognitive impairment. *Clin. Neuroradiol.* **30**(3), 559–568 (2020).
38. Liu, Y. et al. Multimodal characterization of gray matter alterations in neuromyelitis optica. *Mult. Scler.* **24**(10), 1308–1316 (2018).
39. Yang, Y. et al. Cerebellar connectome alterations and associated genetic signatures in multiple sclerosis and neuromyelitis optica spectrum disorder. *J. Transl. Med.* **21**(1), 352 (2023).
40. Crossley, N. A. et al. The hubs of the human connectome are generally implicated in the anatomy of brain disorders. *Brain* **137**(Pt 8), 2382–2395 (2014).
41. Huang, M. et al. Synchronization within, and interactions between, the default mode and dorsal attention networks in relapsing-remitting multiple sclerosis. *Neuropsychiatr. Dis. Treat.* **14**, 1241–1252 (2018).
42. Guo, X. et al. Altered neurovascular coupling in neuromyelitis optica. *Hum. Brain Mapp.* **40**(3), 976–986 (2019).
43. Savoldi, F. et al. Functional brain connectivity abnormalities and cognitive deficits in neuromyelitis optica spectrum disorder. *Mult. Scler.* **26**(7), 795–805 (2020).

Acknowledgements

This work was supported by the program for National Natural Science Foundation of China (82160331), Jiangxi Province Double Thousand Talent Plan (jxsq2023201039), This project is implemented by the Jiangxi Clinical Research Center for Medical Imaging (20223BCG74001), and Jiangxi Province Key Laboratory of Precision Pathology and Intelligent Diagnosis (2024SSY06281).

Author contributions

X.L.: Conceptualization, data curation, software, writing – original draft, visualization, writing – review & editing. Q.Z.: conceptualization, resources, investigation, data curation. Y.Z.: Methodology, Data curation. Y.W.: Methodology, data curation. T.H.: Methodology, data curation. L.W.: Methodology. M.H.: Data curation. F.Z.: project administration, supervision, writing – review & editing.

Declarations

Competing interests

The authors declare no competing interests.

Additional information

Supplementary Information The online version contains supplementary material available at <https://doi.org/10.1038/s41598-024-84508-8>.

Correspondence and requests for materials should be addressed to F.Z.

Reprints and permissions information is available at www.nature.com/reprints.

Publisher's note Springer Nature remains neutral with regard to jurisdictional claims in published maps and institutional affiliations.

Open Access This article is licensed under a Creative Commons Attribution-NonCommercial-NoDerivatives 4.0 International License, which permits any non-commercial use, sharing, distribution and reproduction in any medium or format, as long as you give appropriate credit to the original author(s) and the source, provide a link to the Creative Commons licence, and indicate if you modified the licensed material. You do not have permission under this licence to share adapted material derived from this article or parts of it. The images or other third party material in this article are included in the article's Creative Commons licence, unless indicated otherwise in a credit line to the material. If material is not included in the article's Creative Commons licence and your intended use is not permitted by statutory regulation or exceeds the permitted use, you will need to obtain permission directly from the copyright holder. To view a copy of this licence, visit <http://creativecommons.org/licenses/by-nc-nd/4.0/>.

© The Author(s) 2025